Laser Cladding With Combined NIR and Blue Diode Laser Including In-Line Atomic Emission Spectroscopy

Malte Schmidt[1] · Robert Köhler[2] · Christoph Gerhard[2,3] · Knut Partes[1]

Abstract

For Directed Energy Deposition processes (DED) lasers in the near infrared (NIR) as well as in the infrared (IR) range are predominantly used. Recent developments have also made high-power lasers in the visible spectrum available. As the DED process is used for cladding of surfaces, repairing and additive manufacturing of components, process monitoring and control methods are necessary to ensure a consistent manufacturing quality. Optical emission spectroscopy (OES) of the process radiation can provide information on process conditions and the deposition layer during DED processes. However, DED processes are in the heat conduction regime and superimposed broad spectral emissions dominate the wavelength specific signals. The object of this work is to compare the process behavior using a NIR and blue diode laser separately as well as in combination. The influence of the laser wavelength on the cladding result as well as on the emitted process radiation is to be determined. Therefore, single tracks of Co-based powder (MetcoClad21) were clad on an S235 base material by using each laser source separately as well as in combination. Both laser beams were combined within a single hybrid optic. While the scan speed and powder feed rate remained constant, the laser power was varied. Single spectra have been recorded from the process using a spectrometer. Single spectra are sorted and element lines were identified. Only non-ionised elements could be detected, with chromium appearing frequently. It was shown that comparable results in terms of cladding quality can be produced independently from the laser wavelength. In fact, less laser power (app. 30% less, 1 kW at 980 nm (NIR) compared to 0.7 kW at 450 nm (blue)) was needed aiming for comparable results in geometrical factors (as dilution, height, depth, width) and homogeneity (chemical composition distribution) by using blue laser irradiation. Furthermore, more spectrometric signals (approx. 2–28 times more) were detected compared to experiments using only NIR irradiation with the same laser power. This effect is particularly high at low laser powers and decreases with increasing power. Hence, it is possible to enable in-line process analysis by adding blue laser irradiation to the mix of the beam.

Extended author information available on the last page of the article

Introduction

Overview About Directed Energy Deposition Processes

Directed Energy Deposition (DED) can be used in a wide range of different applications such as cladding of surfaces [1, 2] as well as the repairing [3, 4] and additive manufacturing of parts [5, 6]. In this process, a high-power laser generates a melt pool on the surface of a metallic material, and filler material (commonly in powder form) is simultaneously delivered into the melt pool. By controlling the material flow and the laser power, functional layers can be placed on surfaces by putting tracks side by side. Due to the large number of available powder materials, the process can be used quite flexibly [7]. For instance, high entropy alloy powder can be used as filler material for lap joints with dissimilar alloy configuration [8]. In order to achieve consistent quality during DED processes, numerous monitoring and control methods have been developed. Contact-less temperature measurement during laser cladding was performed by Köhler et al. using a CMOS-based camera with spatial emissivity compensation [9]. Doubenskaia et al. used an infrared camera to restore temperature profiles on the melt pool surface using emissivity values and brightness temperatures provided by the raw camera signal [10]. Further investigations on temperature measurements during laser cladding have been conducted by Bi et al. [11], Song et al. [12], Altenburg et al. [13] and Thawari et al. [14]. Multiple monitoring and inspection techniques for metal-based additive manufacturing process, incl. DED, have been reviewed by Chua et al. [15]. A multi-sensor monitoring for DED additive manufacturing was investigated by Chabot et al. [16] combining thermal and geometrical control loops. Buhr et al. used a line projecting laser and CMOS sensor to measure the layer high during a robot-guided laser metal deposition (LMD) process, also known as DED [17].

Optical Emission Spectroscopy (OES) in Laser Welding Processes

A specific field of process monitoring methods is the analysis of optical process emissions. Optical emission spectroscopy (OES) was already investigated in several laser processes like DED and laser deep penetration welding processes. In the field of laser deep penetration welding, the determination of the chemical composition [18], homogeneity [19] and detection of defects [20–23] were focused. OES has also been investigated for similar applications in DED processes. A lack-of-fusion defect detections was investigated for titanium alloy layers [24]. Data of multiple sensors, including spectroscopic measurements of the process emissions, were combined with X-ray computed tomography data using machine-learning algorithms. It could be shown that process parameter such as laser power, powder flow rate, and hatch pattern have a statistically significant effect on the length of pores. The

sensor system is capable of predicting lack-of-fusion defects across a layer. Further investigations on defect detection have been performed [25, 26]. By using databases containing atomic emission lines, for example the NIST Atomic Spectra Database [27], measured spectral peaks can be identified. For instance, the detection of Cr spectral lines in the course of DED processes has been investigated. It could be confirmed that emission spectroscopy can be used as an in situ monitoring system with lower laser powers [28]. The loss of chromium during the direct metal deposition of the Ni-based alloy 718 was investigated by Kisielewicz et. al. Optical emission data were measured from the plasma plume above the melt pool with increasing laser power. Multiple Cr I spectral lines have been identified. Specimens, built with higher laser power, showed a lower Cr content related to those built with lower laser power. The intensity of Cr lines increases with higher laser power. Higher energy input led to increasing vaporisation and the depletion of Cr atoms from the melt pool [29]. Similar effects could be observed during a recently published study [30]. Co-Cr-powder was cladded on mild steel substrate with a coaxial powder nozzle and a 4 kW diode laser. Cr I lines as well as Mn I- and Co I lines could be detected. The intensity and incidence of detected element lines correlated with an increase of laser power. The Cr-content was not measured during these experiments. Within the spectrometric data, the peak with the highest intensity was always found at a wavelength of 520.6 nm or 520.7 nm (based on spectrometer resolution). According to the data provided by the NIST Atomic Spectra Database [27], this peak could probably be assigned to three closely spaced Cr I emission lines. This prediction was confirmed by a subsequent study using the same laser cladding system and powder material. For the spectrometric measurement a high-bandwidth/medium-resolution and a narrow-bandwidth/high-resolution spectrometer were used simutaniously [31]. Due to the high-resolution spectrometer the single peak at 520.7 (provided by the high-bandwidth spectrometer) could be clearly resolved in the three previously assigned Cr I emission lines. This specific peak at 520.6 nm or 520.7 nm has also been found and assgined to Cr I during SLM/PBF processes using OES. Dunbar and Nassar investigated the line-to-continuum ratio using the intensities of the Cr I peak at 520 nm and the continuum emissions around 530 nm using bandpass filters and photodiodes [32]. Therefore sample parts were build with a PBF system using Inconel 718 powder. X-ray computed tomography was used to determine the percentage of void within the built up samples. The line-to-continuum ratio could be related to the percentage of void within the final part. Lough et al. used OES (especially Cr I emission line at 520.6 nm or 520.7 nm) during SLM process [33]. It has been shown that the intensity of the Cr I emissions correlated with the melt pool size. The intensity of spectral emissions is also influenced by the build chamber athmosphere and pressure.

Monitoring of the chemical composition DED processes were investigated in several studies. Real-time Cr measurements have been performed by using spectral line intensity ratios of neutral Cr and Fe lines. The element contents are determined by calibration curves, based on previous experiments. Approaches for element content prediction using the detection of plasma temperature or electron density occurred to be less accurate [34]. The monitoring of nickel and chromium content had also been performed using line ratios of specific neutral Ni and Cr lines. The prediction

calibration curve was built through multiple experiments using different powder materials with varying Ni content [35]. In order to expand the quantity of elements to be measured, Wang and Liu used four different Ni-based alloy powders on an Fe-based substrate. Calibration curves for different elements were generated by correlating the weight ratio and the line intensity ratio of two elements. The prediction showed quite suitable results, although elements with lower concentration within the alloy could be measured with a much lower accuracy [36]. The prediction of Al content within an Al-Ti-powder deposited layer was performed in [37] with four different methods. Accuracy and stability of element concentration prediction of each method was focused on the frame of this study. The methods to be compared are calibration curves, artificial neural network (ANN), partial least square regression (PLSR), and support vector regression (SVR). It has been observed that SVR using line intensity and integrated intensity data provides an improved performance for predicting the Al concentration compared to the other three methods.

Every referred study that has dealt with spectrometric measurements has used conventional NIR (diode, disk, fibre: 900–1100 nm) or IR (CO_2:10.6 μm) lasers for their experiments. Thus, the influence of shorter laser wavelengths on the spectrometric measurements could not yet be shown.

As DED processes are in the heat conduction regime and superimposed broad spectral emissions dominate the wavelength specific signals, improving the detectability of element specific emissions using shorter laser wavelengths is intended. However, the process and the deposition track should not be negatively influenced by this. Laser welding with irradiation in the visible field, including mixing with conventional NIR lasers, is mainly used for welding high reflective materials as for example copper [38–42]. Furthermore, systems with two separate spots for lapped joints are also used [43, 44]. The impact of laser wavelength and process parameters during laser cladding on emission spectra and cross-sectional-dimensions of the deposition tracks was thus investigated in the present work where the simultaneous application of two quite different laser sources and wavelengths, respectively, to a DED process was investigated for the first time. As summarised in the following section, this approach was chosen in order to gain more information on laser-matter interactions and the accompanying potential for the enhancement of such processes.

Laser-Material Interaction

The technological approach investigated in this work, i.e. the mixing of blue and near infrared (NIR) laser irradiation, is based on the expectable differences in laser cladding material interactions and the accompanying differences in terms of melting. Generally, such interactions depend on quite a number of parameters as for example the particle size as well as absorption and reflexion characteristics of the cladding material. Since the size or diameter of powder particles governs the type and direction of scattering, the particle size distribution of the used cladding material was determined via granulometric analysis according to ISO 2591. As shown in Fig. 1, it turns out that in most instances, the particles are larger than 45 μm.

Fig. 1 Particle size distribution of the cladding powder raw material (MetcoClad 21) used in the present work
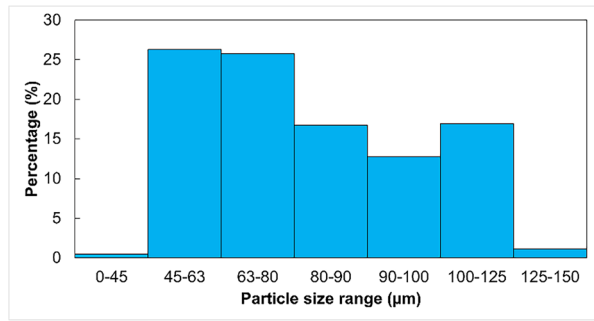
Since the particle size (45–150 μm) is thus some order of magnitudes higher than both applied laser wavelengths (450 nm, 980 nm), pure optical scattering occurs; the incident laser light is thus predominantly scattered forward in both cases [45, 46]. A much higher wavelength-dependency and thus noteworthy impact on laser light-particle interaction becomes evident when comparing the optical properties of the powder's main elements (Co and Cr) as well as the main element of the substrate (Fe), see Fig. 2. Laser radiation, i.e. electromagnetic waves, can be absorbed or reflected by opaque materials such as metals via interaction with free electrons within the "electron gas". Besides the temperature, surface roughness, and the angle of incidence (AOI) of light, the absorption of a material is mainly affected by the radiation wavelength and its polarisation. Due to the curved and moving and thus chaotic surface of the melt pool in the
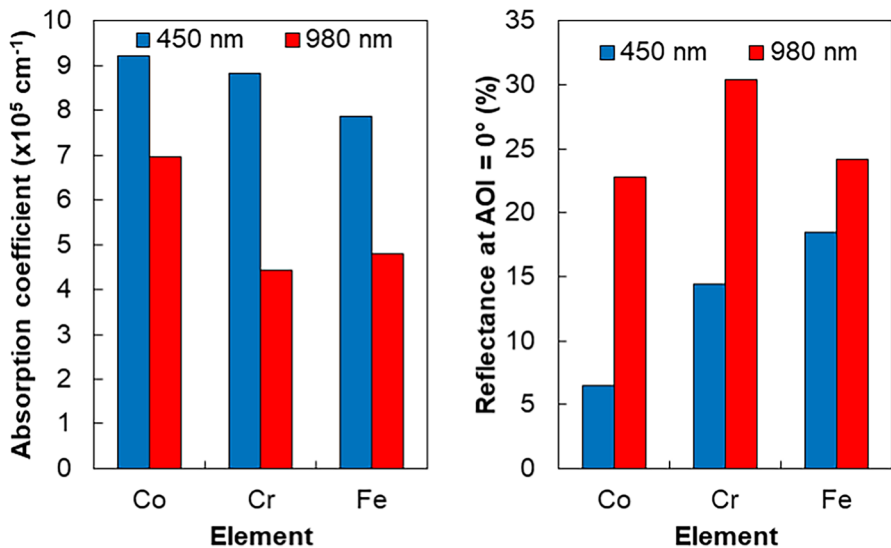

Fig. 2 Absorption coefficient (left) and reflectance at normal incidence, i.e. an angle of incidence (AOI) of 0° (right), of the main compounds of the cladding powder raw material (Co and Cr) and the substrate (Fe); data taken from [47]

DED process, the AOI is considered 0° in this theoretical analysis. For some metals a rise in material temperature leads to decreasing reflectivity and increasing absorptivity.

Laser radiation with shorter wavelength contains of photons with higher energy. A greater number of electrons can absorb these higher energetic photons which lead to decreasing reflectivity and increasing absorptivity [45]. For all elements the absorption coefficient is about 1.3- to 2-times higher in case of blue laser light at 450 nm when compared to NIR laser irradiation at 980 nm [47]. This might consequently lead to an improved energy coupling of incoming laser light into the particle and substrate material when applying the blue laser source. Moreover, higher reflectance and thus losses at the particle and substrate surfaces occur in case of NIR wavelengths. In the present case, such reflexion losses can be anticipated to be 1.3- to 3.5-times higher in comparison to the blue laser wavelength.

Finally, the application of such laser irradiation of shorter wavelength could lead to an improved melting of the cladding material and the underlying substrate due to an increased absorption and decreased surface reflexion of the used cladding materials. Consequently, laser cladding applying blue lasers could provide comparable results, like deposition track dimensions and element distribution, as for cladding processes with NIR lasers, but require less energy or power. However, it must be ensured that the chemical composition of the deposition track is not changed by the increased absorption, in the form of increased evaporation of alloying elements.

Methodology

Experimental Setup

DED experiments were performed using an NIR (980 nm) and a blue (450 nm) diode laser source combined within a single robot-guided (Kuka RL 80 6-axis linear robot) processing head. The NIR diode laser source (Laserline-LDF 16,000–60) has a maximum output power of 16 kW and a beam parameter product of 66 mm mrad. The blue diode laser source (Laserline-LDM 1500–60 blue) has a maximum output power of 1.5 kW and a beam parameter product of 66 mm mrad. Laser irradiation was delivered separately for each laser source via optical fibres with core diameters of 600 μm (NA 0.2) to the hybrid optic (OTS-5 series by Laserline). For both beams, separate collimating lenses were used. The experimental setup of the processing head can be seen in Fig. 3a. The collimated beams were combined and focused on the substrate surface, resulting in circular spots with approx. Ø1.6 mm diameter and a flat top intensity distribution. Both laser spots and the coaxial powder nozzle (HighNo 5.0 by Harald Dickler – Sonderoptiken für die Lasertechnik GmbH & Co. KG) were aligned to each other in planar and vertical dimensions. Thus, the powder spot with a diameter of Ø 2.0 mm was also focused on the substrate surface. Powder material was provided using a powder feeder system (GTV Verschleißschutz GmbH). For all experiments carrier gas flow was set to 5 l/min and shielding gas flow was set to 12 l/min.
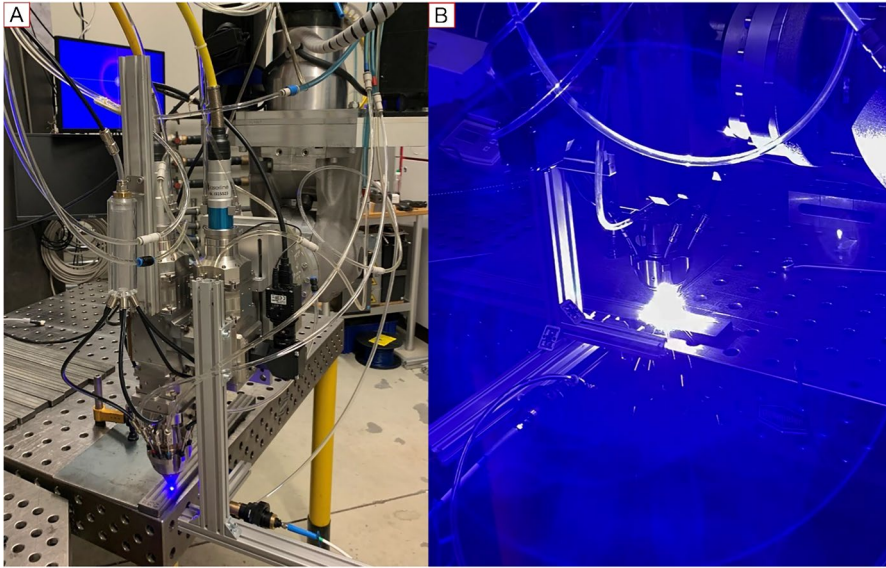
Fig. 3 (**a**) Experimental setup of the processing head and (**b**) DED process using blue diode laser

Experimental Parameters

For each experiment, a single deposition line with a length of 380 mm was placed onto a separate metal plate (400×40x12 mm) made of low-alloyed mild steel (S235). Reference experiments were performed by using only a single laser source – blue or NIR. For the blue diode laser, the power was varied between 0.5 kW and 1.3 kW in steps of 100 W. Using the NIR diode laser, the laser power was varied between 0.6 kW and 1.5 kW in steps of 100 W. Both the scan velocity during processing and the powder feed rate remained static at 1 m/min and 16.8 g/min, respectively. Figure 3b shows the DED process while using the blue diode laser.

In order to investigate the influence of varying laser power distributions, the radiation of both laser sources was combined. Therefore, proportions of each laser source were reduced or increased by steps of 100 W as shown in Fig. 4. The sum of laser powers remained constant at 1.0 kW. As in the reference experiments, single deposition lines were placed onto separate substrate metal plates.

Materials

A stationary metal analyser (Spectrolab, SPECTRO Analytical Instruments GmbH, Kleve, Germany) was used to determine the chemical composition of the substrate material (S235) via arc spark optical emission spectrometry. A substrate material sample was ground with P80 SiC-Paper and cleaned with denatured
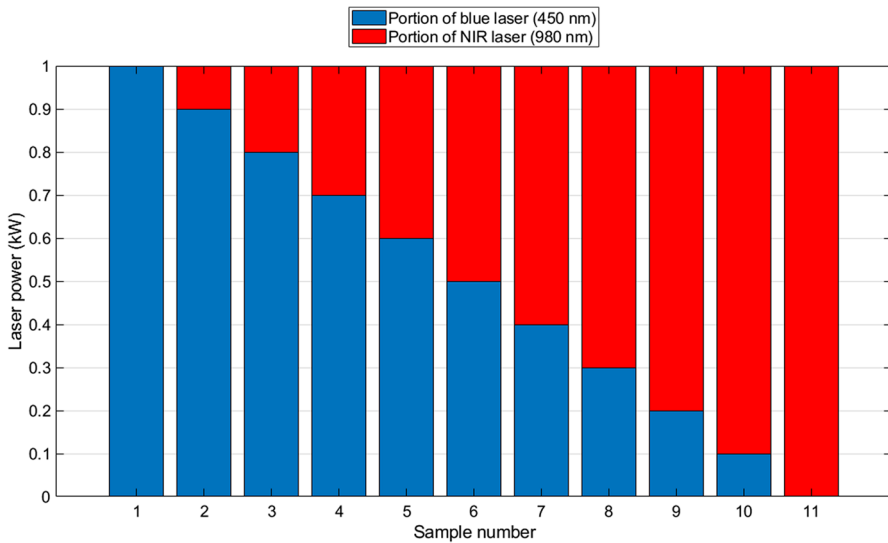
Fig. 4 Particular laser power distributions of blue and NIR laser irradiation at total output of 1.0 kW for laser beam combination experiments

alcohol before each measurement. The analyser was preconfigured for analysis of low-alloyed steel. Analysis results are averaged after three separate measurements and shown in Table 1.

The applied powder material was a cobalt-based alloy (MetcoClad21). Its chemical composition was taken from the batch specific inspections certificate provided by the manufacturer. The values are shown in Table 1.

In addition, the powder particles were visualised using a scanning electron microscope (SEM) (Phillips XL30 TMP, Philips Electron Optics, Eindhoven, The Netherlands). As shown in Fig. 5, the particles are spherically shaped. Smaller particles (satellites) are attached to bigger ones. Due to the shape of the powder particles, a sound flux ability and a stable continuous mass flow could be expected [48, 49].

Spectroscopic Measurements

Spectroscopic signals were recorded using a UV–Vis spectrometer (OCEAN-HDX-UV–VIS, Ocean Insight, Orlando, FL, USA) in the wavelength range of 200–800 nm. The resolution at FWHM is 0.73 nm using a 10 µm entry slit. The measurement setup is illustrated in Fig. 6. Irradiation emitted during the process was collected using a fused silica collimating lens. It was horizontally attached to the processing head, aligned to the optical centre line of the laser beam and orientated perpendicularly to the cladding direction. The lower edge of the collimated beam was set to a 1 mm in respect to the substrate surface. As the blue laser source emits intense radiation at 450 ± 20 nm an edge pass filter (490–900 nm) was placed

Table 1 Chemical composition of substrate material (S235) measured via optical emission spectrometry and powder material (MetcoClad21) provided by manufactures inspection certificate

WT %	C	Si	Mn	Cr	Mo	Ni	Al	Co	Cu	Fe	Trace particles less than 50 ppm and P+S+W
Substrate (S235)	0.10	0.19	1.02	0.03	0.01	0.03	0.03	0.01	0.02	98.56	-
Powder (MetcoClad21)	0.23	0.7	0.8	26.7	5.4	2.7	-	63.15	-	0.1	balance
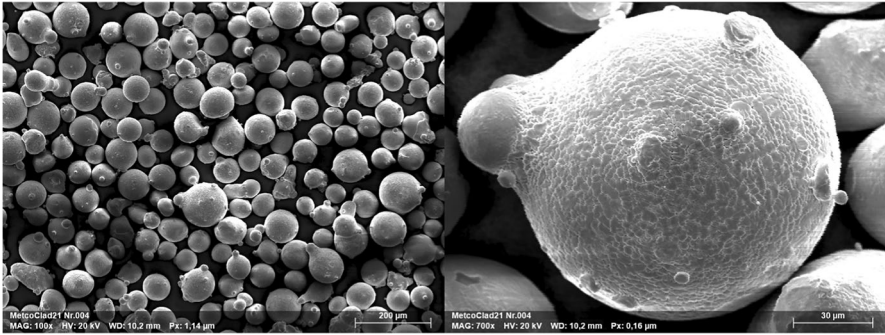
Fig. 5 SEM-imaging of powder particles MetcoClad21
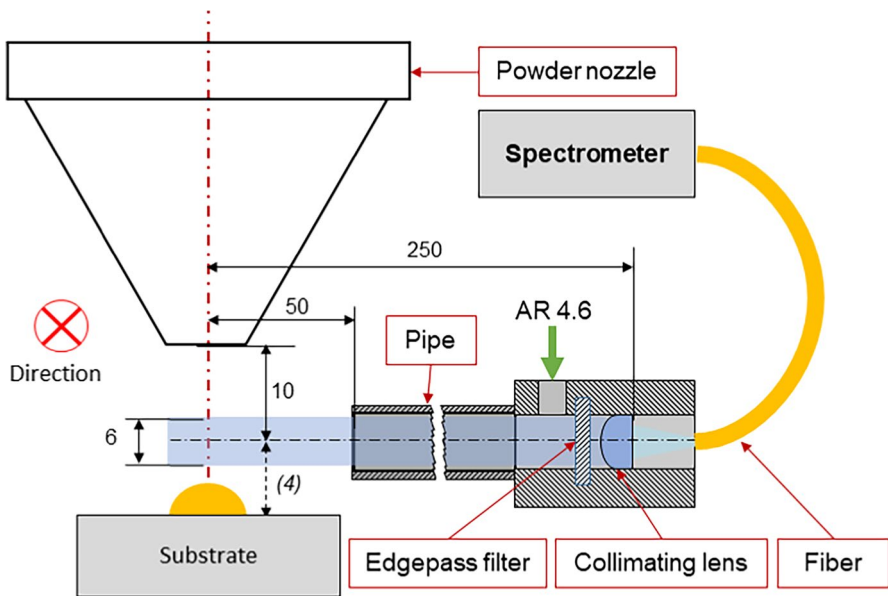
Fig. 6 Spectroscopic measurement setup and alignment

in front of the lens. Due to slight irregularities in the optical density of the filter, a small portion of the blue laser radiation is still visible in the spectra. However, these signals are mostly less intense than the process emissions and therefore do not interfere with the measurement signals. This can be seen in Fig. 7. In the range of 500–550 nm, the optical density of the filter remains almost constant. Minor irregularities are therefore negligible. In order to reduce the impact of scattered light, the collimating lens was attached to a pipe with an inner diameter of 6 mm and a blackened inner surface. The distance between the collimating lens and the optical centre line was set to 250 mm. A moderate shielding gas flow of 1 l/min was applied to the pipe in order to prevent powder particles to contaminate optical components and
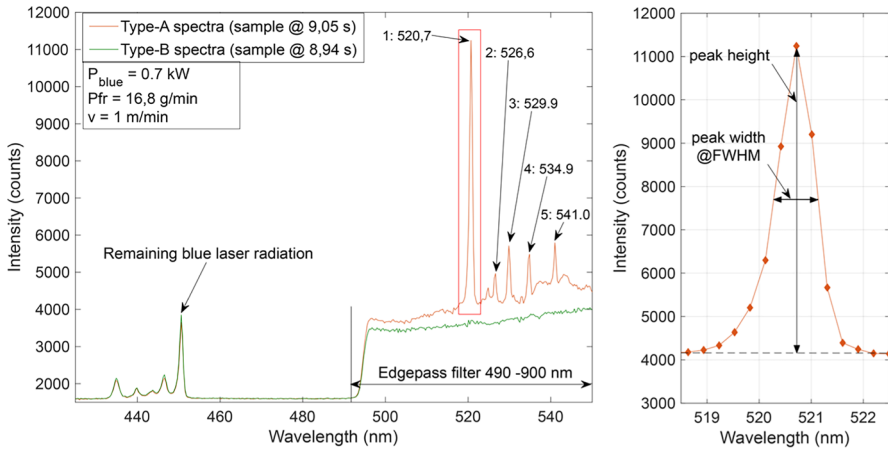
Fig. 7 Type-A/B sample spectra from reference experiments with 0.7 kW blue laser power, 16.8 g/min powder feed rate and 1.0 m/min scan velocity

negatively influence the measurements. A multi-mode fibre with a core diameter of 100 μm was used to connect the collimating lens and the spectrometer.

Single spectra with 10 ms integration time were measured back-to-back resulting in a scan rate of 100 Hz. The readout time within the CCD-detector, performed after each integration cycle, is in the range of several μs and is thus negligibly small. Single spectra are sorted into two categories – Type-A and Type-B. This has been published in previous work [30]. Type-A spectra show at least one detectable peak whereas Type-B spectra merely feature thermal background radiation without any detectable peaks. Single spectra were analysed by a build in MatLab function "findpeaks" parameterised as followed:

- Minimum peak height: 500 counts
- Peak width at FWHM: > 0,73 nm up to maximum of 3 nm

Peak height is defined as the amount of counts between the peak tip and the background radiation. Figure 7 shows a typical Type-A (orange plot) and Type-B (green plot) spectrum as well as an exemplary peak height and width measurement. Within Type-A spectra element lines can be identified and assigned to specific element atomic emission lines with the aid of the NIST Atomic Spectra Database [27]. In order to compare the evaluability of the spectrometric signals for different experiments, the ratio of Type-A spectra is calculated according to

$$Ratio_{Type-A} = \frac{n_{Type-A}}{n_{Type-A} + n_{Type-B}} \tag{1}$$

where n_{Type-A} corresponds to the amount of all Type-A spectra and n_{Type-B} corresponds to the amount of all Type-B in an experiment.

Metallographic Analysis

In order to analyse the deposition track geometry, samples have been cut and ground with SiC-paper. First polishing was performed using a 3 μm diamond suspension and subsequent fine polishing was carried out using 0.05 μm colloidal silica suspension. Cross-sections were not etched, as the dilution is clearly visible due to the different materials. Images of each cross-section were taken using a microscope (Leica DM2700M, Leica Microsystems GmbH, Wetzlar, Germany) with a 50×magnification. Cross-sectional-dimensions, including deposition track height, width, weld-in depth and molten areas underneath and above the substrate surface were measured within these images. The dilution derived in this vein describes the ratio D between the molten area below the substrate surface A_1 and the sum of all molten areas $A_1 + A_2$ of the deposition track according to

$$D = \frac{A_1}{A_1 + A_2}. \tag{2}$$

For each deposition track sample three separate cross-sections have been made. Value for deposition track height, depth, width and dilution are averaged from these three measurements. Error bars shown in Figs. 8 and 10 represent the minimum and maximum values of the measurements.

XPS Measurements and Analysis

The chemical composition of the cladding surfaces was determined via high-resolution X-ray photoelectron spectroscopy (XPS) using a monochromatic Al-K$_\alpha$ source with a photon energy of 1486.6 eV. The used apparatus (model PHI VersaProbe II from Ulvac-phi, Inc., Osaka, Japan) is operated at a base pressure of $2{\bullet}10^{-6}$ Pa at room temperature; it was calibrated to copper and gold standards at an electron energy of 932.62 eV and 83.96 eV, respectively. High-resolution spectra of carbon (C1s), oxygen (O1s), iron (Fe2p), chromium (Cr2p), molybdenum (Mo3d) and cobalt (Co2p$_{1/2}$) were detected with an X-ray power of 25 W, a beam diameter of 100 μm, a pass energy of 46.95 eV and a step size of 0.1 eV at a constant electron take-off angle of 45°. To avoid charging effects on the sample surfaces, neutralisation was carried out with a cool cathode electron flood source and low-energy argon ions. Finally, data analysis was executed with the aid of appropriate software (MultiPak, version 9.9 from Ulvac-phi, Inc.). The measured spectra were fitted applying Voigt profiles after performing a Shirley-type baseline subtraction.

In order to obtain depth-resolved information of the samples, cross-section ground samples were alternately measured and sputtered where 12 measuring points were defined over an overall measuring depth of 1,900 μm. The distance between the individual measuring points was 200 μm in the near-surface range from 200 μm to 600 μm and within the bulk material at a depth from 1100 μm to 1900 μm. For higher depth resolution, the measuring increment was reduced to 100 μm in the transition region from the powder cladding to the bulk material, i.e. at a depth range between 600 μm to 1000 μm. For the alignment of the cross-section ground samples, X-ray images (SXI; X-ray beam induced secondary electron images) were taken where the centre of the X-ray beam was aligned to the

outermost surface of the cladding for acquiring the first measurement point. To remove impurities induced in the course of sample preparation via cross-section grinding, two sputter cleaning processes with argon ions were performed. First, the surface was sputtered for 10 min at an ion energy of 3 kV where the sputtered area was 3×3 mm^2, centred to the measurement point at 600 µm. Second, sputtering was carried out before each measurement for each point for 1 min at 1 kV and an area of 3×3 mm^2.

Results and Discussion

Cross-Sectional-Dimensions and Spectroscopic Analysis

Line Identification

Due to the large number of spectra, not all of them can be investigated individually. Therefore, the identification of characteristic lines was performed by investigating a sample Type-A spectrum, seen in Fig. 7. The spectrum was recorded during reference experiments with 0.7 kW blue laser power, 16.8 g/min powder feed rate and with a velocity of 1 m/min at 9.05 s into the process. At this time, the track has covered 150.8 mm of its 380 mm travel. All peaks located by the software are numbered and shown in Table 2 with the observed wavelength. Peaks could only be detected in the region between 520.7 nm and 541 nm. The region below 490 nm was cover by the edgepass filter, blocking the blue diode laser irradiation at 450 nm. Above 550 nm no detectable peaks could be found. By the use of NIST Atomic Spectra Database [27] the most applicable element lines are selected and assigned to the observed peaks.

As it can be seen in Table 2, the observed peaks probably consist of several Cr I and a single Fe I elemental line. Other elements that are not considered in the present work (due to chemical composition analysis) are neglected. The most prominent peak (No. 1)

Table 2 Observed peaks as well as corresponding element lines including the corresponding energy levels. Data taken from NIST Atomic Spectra Database [27]

Peak No	Observed Wavelength (nm)	Element Line (nm)	Energy Levels $E_i - E_k (cm^{-1})$	Line Ref
1	520.7	520.44981 (Cr I)	7593.1484–26,801.9009	[50]
		520.60229 (Cr I)	7593.1484–26,796.2691	
		520.84094 (Cr I)	7593.1484–26,787.464	
2	526.6	526.57143 (Cr I)	7810.7795–26,796.2691	[50]
		526.7270 (Fe I)	35,257.324 – 54,237.213	[51]
3	529.9	529.66905 (Cr I)	7927.441–26,801.9009	[50]
		529.82715 (Cr I)	7927.4–26,796.3	
		530.07451 (Cr I)	7927.4–26,787.5	
4	534.9	534.57959 (Cr I)	8095.2–26,796.3	
		534.83141 (Cr I)	8095.2–26,787.5	
5	541.0	540.97834 (Cr I)	8307.6–26,787.5	

measured at 520.7 nm is composed of the three closely neighboured Cr I transitions at 520.44981 nm, 520.60229 nm, and 520.84094 nm. This has been verified due to a previous published study [31]. The first two of these lines are known to be asymmetric [27], explaining the slight asymmetry of the observed line. Peak (No. 2) was assigned to a Cr I transition at 526.57143 nm and a Fe I transition at 526.7270 nm. As this peak consists of two different elements it is much more difficult to use it for analysis. The remaining peaks can also be assigned to Cr I lines. Thus, only non-ionised lines were found.

Laser Cladding Using Exclusively NIR or Blue Laser Irradiation

The aim of the reference experiments presented in this section is to show how the two different applied laser wavelengths affect both the spectrometric measurements and the process result. All cross-sections were examined and measured where no pores or cracks could be found. Figure 8A shows the ratio of Type-A spectra. In Fig. 8B-D three cross-sectional-dimension parameters for increasing laser power of both wavelengths are shown. These parameters describe the deposition track dilution (B), height and depth (C) as well as the width (D). With increasing laser power, the ratio of detected Type-A spectra during the process increases for both laser wavelengths. However, blue laser irradiation shows significantly higher ratios compared to NIR irradiation at equal laser powers. A similar trend can be seen for the deposition track dilution in Fig. 8B even though the difference between blue- and NIR-irradiation decreases with increasing laser power. The deviation of minimum and maximum values from the averaged dilution is also very small for both laser wavelengths. The deposition track height (Fig. 8C) is similar for both wavelengths in case of lower laser power (0.7–0.8 kW). With increasing laser power, the height for NIR irradiation remains mainly constant, although a slight increase can be observed from 1.3 kW. Slightly higher tracks can be produced when blue irradiation is used. This could be due to the increased absorption coefficient of blue laser irradiation with the used powder and substrate material, which lead to an increased powder catchment efficiency. In contrast, higher welding depths are observed with increasing laser power for both wavelengths. However, depositions tracks produced by blue laser irradiation show significantly deeper melting areas at similar laser powers. The difference between the averaged depth values remains almost constant at 0.22 ± 0.02 mm in the range between 0.7 kW and 1.3 kW. Due to the small deviations of the height and depth measurements from the averaged values, the error bars in Fig. 8 are partly not visible. The width of the deposition track (Fig. 8D) increases with increasing laser power for both NIR and blue irradiation. This is due to a larger melt pool created by the higher laser power. For laser powers of 0.7 and 0.8 kW the averaged widths are comparable for both laser wavelengths. However, tracks applied with NIR laser radiation with a power of 0.9 kW and above are slightly wider than those with the same amount of blue laser power. The average difference in width for all laser powers between 0.9 kW and 1.3 kW is 0.12 ± 0.02 mm. This could be due to a slight deviation in the focusing and thus the size of both laser spots. In addition, the minimum and maximum values vary for several width measurements, but remain within an acceptable range.

In comparison, deposition tracks with similar cross-sectional-dimensions can be achieved for both laser radiation wavelength. For example, using 1.0 kW NIR laser power results in a deposition track with an averaged dilution of 0.27, track height of 0.48 mm,

melted area depth of 0.30 mm and a width of 1.73 mm. These values can nearly be achieved with only 0.7 kW blue (dilution: 0.23, height: 0.51 mm, depth: 0.25 mm, width: 1.49 mm). Slight deviation in the focusing and thus the size of both laser spots probably leads to a greater deviation in width. Cross-sections of both examples are shown in Fig. 9 (B: 1.0 kW NIR; C: 0.7 kW blue). Additionally, also cross-sections for 1.0 kW blue (D) and 0.7 kW NIR (A) are shown. Here it can be seen that 1.0 kW blue leads to a significantly higher dilution while 0.7 kW NIR shows almost no melted area below the substrate surface. Besides the lower laser power requirement, the amount of identified Type-A spectra is significantly higher while the use of blue laser radiation in contrast to higher NIR laser power.
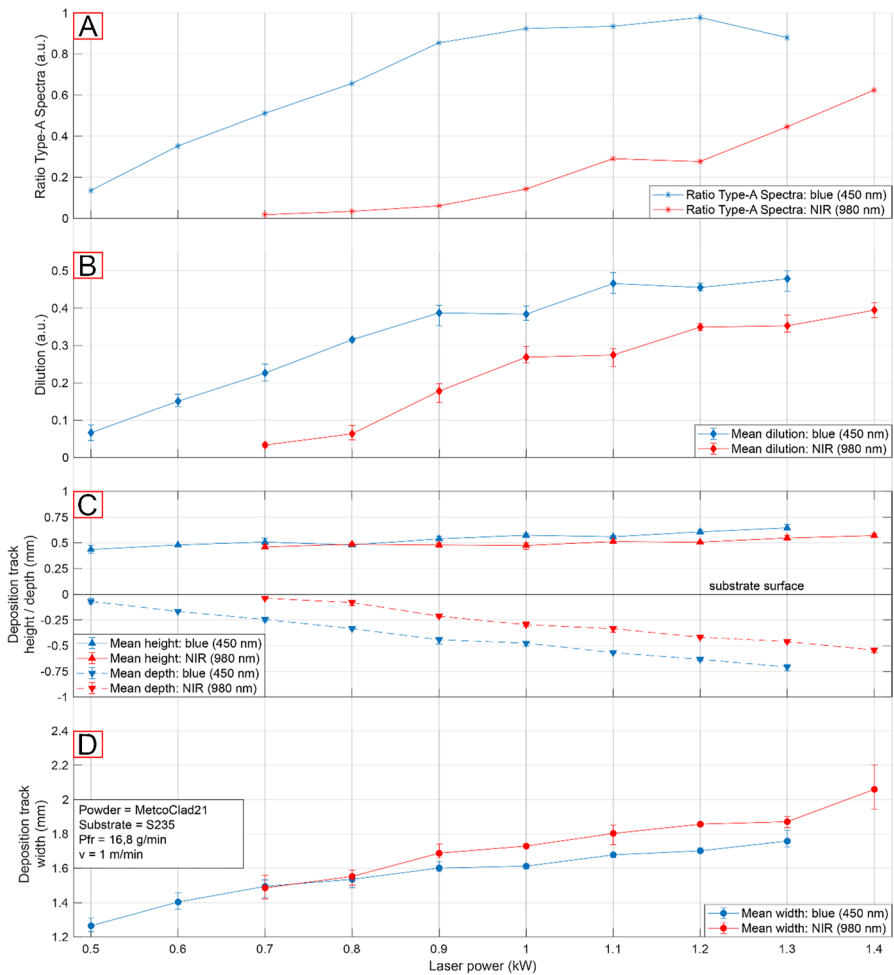
Fig. 8 Type-A-spectra ratio calculated according to Eq. (1) and cross-sectional-dimensions for reference experiments with only one laser source at a time (blue or NIR). Power output is increased by 0.1 kW steps. Powder feed rate of 16.8 g/min and a scan velocity of 1.0 m/min are set. Cross-sectional-dimension values were averaged from three separate cross-sections. The error bars represent the minimum and maximum values of the measurements
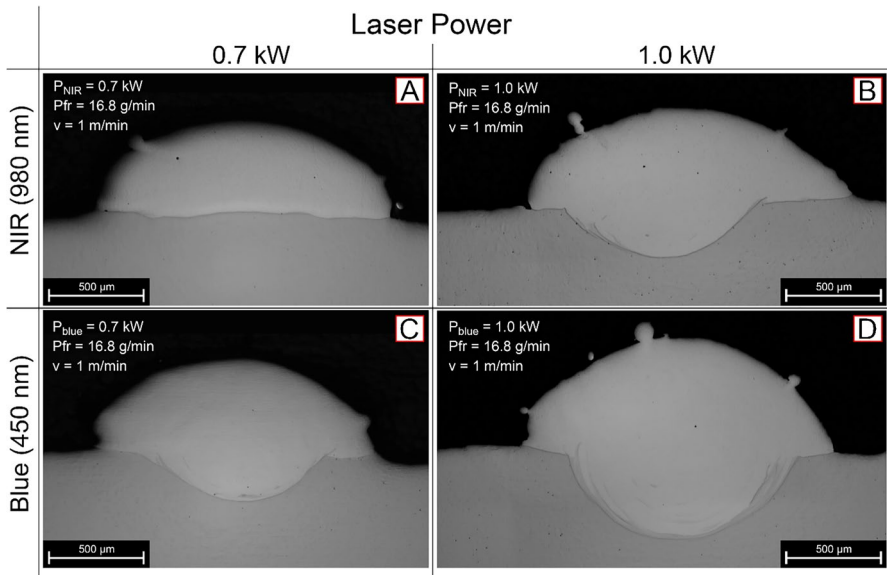
Fig. 9 Cross-sections for blue and NIR laser source at 0.7 kW and 1.0 kW with powder feed rate of 16.8 g/min and a scan velocity of 1.0 m/min. A:(P_{NIR} = 0.7 kW), B:(P_{NIR} = 1.0 kW), C:(P_{blue} = 0.7 kW), D:(P_{blue} = 1.0 kW)

Laser Cladding Using Combined NIR and Blue Laser Irradiation

Thanks to the used hybrid laser optic, it is possible to merge both blue and NIR laser beams at different particular powers. All cross-sections produced in that vein were examined and measured. No pores or cracks could be found. Figure 10 shows, according to the same pattern used in Fig. 8, the ratio of identified Type-A spectra during the experiments, the dilution, the deposition track height, the melted area depth and depositions track width. However, the shown experimental results start at 1.0 kW of NIR irradiation and end at 1.0 kW blue laser light. In between, the proportion of blue/NIR laser power increases (blue) or decreases (NIR) by 0.1 kW per experiment. The results shown for 1 kW NIR are the same as those of the reference experiments in Fig. 8.

Figure 10A shows the ratio of Type-A spectra, which increases with rising proportion of blue laser power significantly. From 0.8 kW blue laser power, the ratio of Type-A spectra increase only slightly up to a maximum of 0.89 at 0.9 kW. It drops slightly to 0.86 at 1.0 kW. As already seen in Fig. 8A by using blue laser irradiation, more Type-A spectra can be measured. By increasing the proportion of blue laser power at a constant total power, this effect could be expected. Similar to the Type-A ratio the dilution (Fig. 10B) increases with increasing proportion of blue laser power. Beginning at an average dilution of 0.27 the melted area under the substrate surface grows as well as the track depth, shown in Fig. 10C. Against this, the area above the surface remains almost constant at 0.62 ± 0.04 mm^2, as also the tracks height at 0.51 ± 0.04 mm
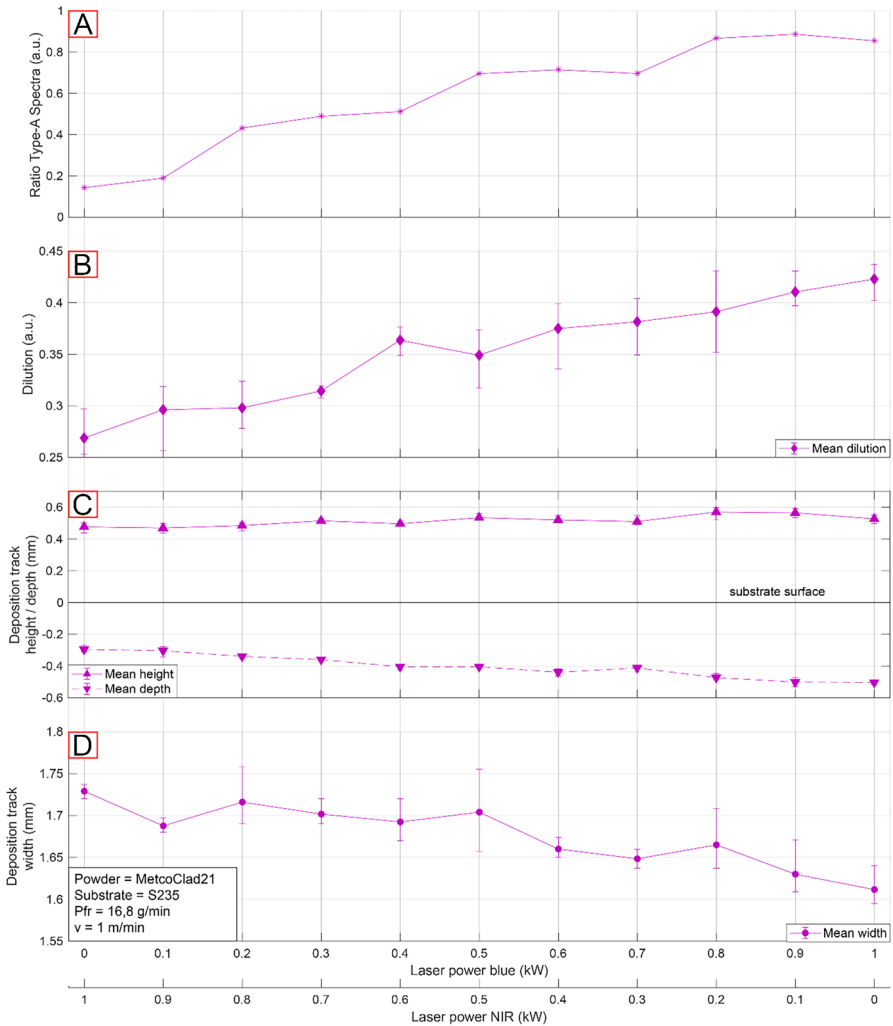
Fig. 10 Type-A spectra ratio calculated according to Eq. (1) and cross-sectional-dimensions for beam combination experiments with both laser sources simultaneously (blue and NIR). Total power output remains static at 1 kW with varying proportion of blue and NIR. Powder feed rate of 16.8 g/min and a scan velocity of 1.0 m/min are set. Cross-sectional-dimension values were averaged from three separate cross-section. The error bars represent the minimum and maximum values of the measurements

for all measured cross-sections (Fig. 11). Figure 10D shows the decrease in deposition track width with increasing portion of blue laser power. Starting at 1.73 mm mean width at 1 kW laser power NIR the tracks narrow to 1.61 mm at 1 kW blue laser power. This difference (0.12 mm) is comparable to the differences in width for the values in the previous chapter and can also be ascribed to a slight deviation in the laser spot diameters.
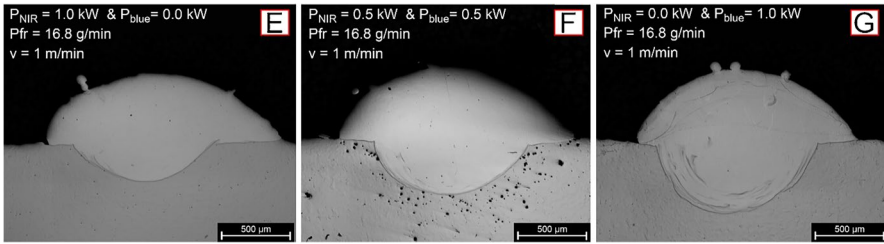
Fig. 11 Cross-sections for beam combination with blue and NIR laser source at total output power of 1.0 kW with powder feed rate of 16.8 g/min and a scan velocity of 1.0 m/min. E:(P_{NIR} = 1.0 kW, P_{blue} = 0.0 kW), F:(P_{NIR} = 0.5 kW, P_{blue} = 0.5 kW), G:(P_{NIR} = 0.0 kW, P_{blue} = 1.0 kW)

Element Distribution

Apart from visual inspection using light microscopy, the prepared cross-sections were also investigated via XPS measurements in order to determine the degree of elemental mixing of the cladding powder and the substrate material as a function of the used laser sources in terms of wavelength and power. Therefore, and as a representative value of mixing or dilution, the ratio R of the powder (Cr, Mo, and Co) and the substrate material (Fe) was determined on the basis of the elemental concentrations C according to:

$$R = \frac{C_{Cr+Mo+Co}}{C_{Fe+Cr+Mo+Co}} \tag{3}$$

In addition to these elements, a certain amount of carbon and oxygen of approximately 5 up to 10 atom-% in total was detected. These elements were, however, not considered for the calculation of the ratio *R* since carbon may be present in both the cladding and substrate material and oxygen can be introduced via oxidation processes from the ambient air during the cladding process. The determined depth-resolved ratios were fitted applying a basic Boltzmann sigmoid function [52]. Figure 12a) shows the ratio as a function of depth for cladding seams produced in three
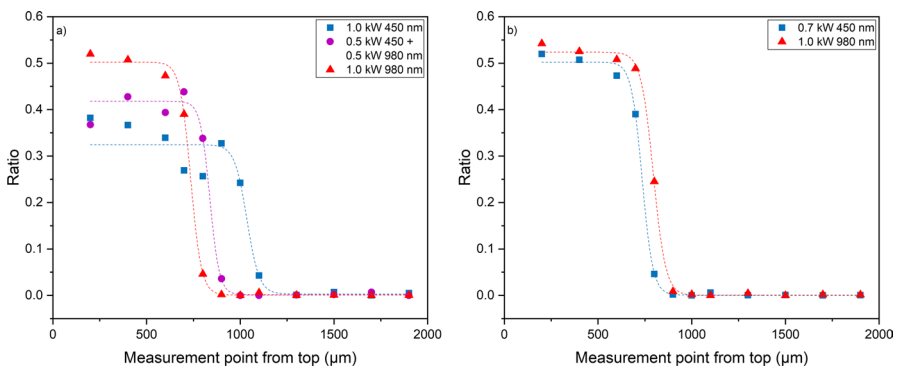

Fig. 12 Ratios of powder and substrate material as calculated according to Eq. (3) vs. depth for different kinds of laser irradiation (**a**); comparison of ratios obtained for irradiation with 0.7 kW at 450 nm and 1 kW at 980 nm, respectively (**b**)

Fig. 13 Interface point of 50% threshold of the fit function for the ratio of powder to substrate materials vs. applied power of the used laser sources
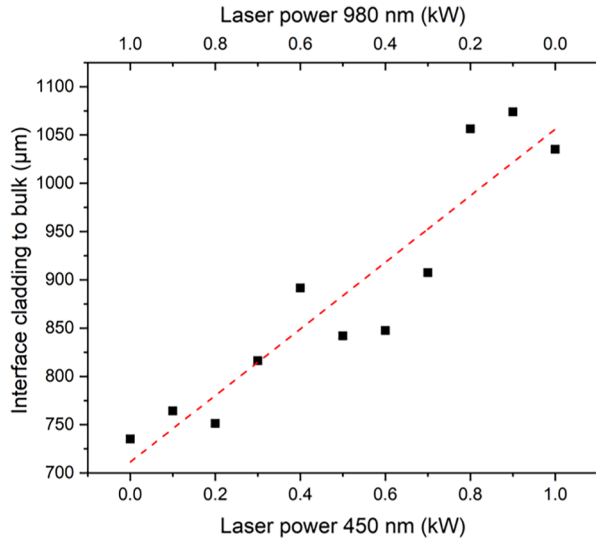
different ways, (i) by applying 1 kW at 450 nm, (ii) by applying 1 kW at 980 nm and (iii), by mixing laser irradiation at both wavelengths in equal shares of 0.5 kW each.

In general, a mixing of the powder with the substrate material was obtained in all cases. It can moreover be stated that the highest depth of the molten zone was achieved when applying merely blue laser light at 450 nm (see Fig. 13). Since in this case the lowest ratio R is observed, the highest dilution of substrate and powder material occurred additionally. Both the dilution and the depth decrease with increasing share in NIR laser light at 980 nm. It can thus be said that the use of lower wavelengths is advantageous in comparison to NIR lasers as also visualised by Fig. 12b. Here, the ratio vs. depth for a laser power of 0.7 kW at 450 nm and 1 kW at 980 nm is displayed. It can be seen that both the dilution and depth of the molten zone are quite similar. Consequently, the use of a blue laser allows a reduction in required laser power by 30% for obtaining comparable machining results.

Usually, the surface zone of laser cladded layers or seams is partially removed to obtain a functional surface. According to this, the chemical composition was measured 400 μm from the top of the cladding as a function of laser power as shown in Fig. 14.

It turns out that obviously, the chemical composition at this measuring point depends on the particular power fraction or share of blue laser irradiation at 450 nm and NIR laser light at 980 nm, respectively. When increasing the portion of 450 nm irradiation and decreasing the one of 980 nm irradiation, more iron from the substrate is found in the weld seam. Concurrently, the concentration of compounds from the cladding powder material declines. This behaviour also indicates that an increased mixing or higher dilution of the cladding and substrate material is achieved in case of a higher fraction of blue laser light. This observation can be explained by the comparison of the optical properties, see chapter "Laser-Material Interaction". At 450 nm, the absorption coefficient of the involved materials is higher than at 980 nm and the reflectance is considerably lower. Both effects lead to

Fig. 14 Atomic concentration of the main compounds of interest vs. applied power of the used laser sources or wavelengths at 450 nm and 980 nm, respectively, measured at depth of 400 μm from the cladding top
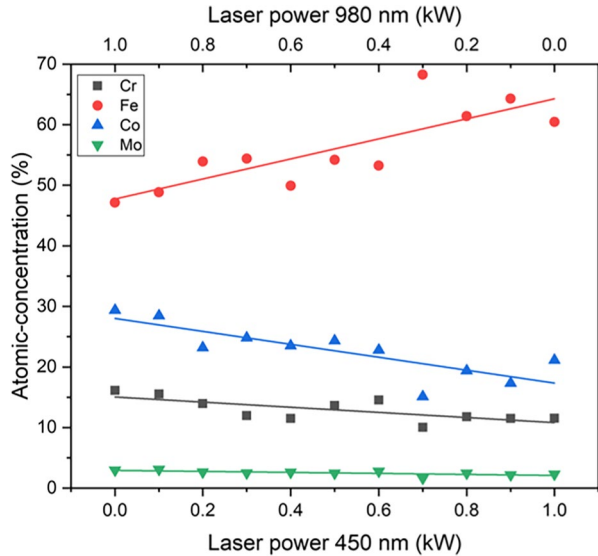
a higher coupling of incoming laser irradiation into the melt zone and thus a higher heating and blending of the melt.

In terms of spectrometric analysability limited portions of blue laser irradiations could increase the amount of analysable Type-A spectra while maintaining similar cross-sectional-dimensions as well as element distribution within the deposition track. As show in Fig. 8, using 1.1 kW NIR laser power results in a dilution of 0.29 and a ratio Type-A spectra of 0.29. A comparable dilution of 0.29 could be achieved with 0.8 kW NIR and 0.2 kW blue laser irradiation, shown in Fig. 10. However, the ratio Type-A spectra increases to 0.43. Also, similar height and depth could be achieved (1.1 kW NIR: 0.51 mm (height) and 0.35 mm (depth) compared to 0.8 kW NIR combined with 0.2 kW blue: 0.5 mm (height) and 0.32 mm (depth). The deposition track width shows a slight difference of 0.13 mm (1.1 kW NIR: 1.85 mm and to 0.8 kW NIR combined with 0.2 kW blue: 1.72 mm). Element distribution, shown in Fig. 14, can be maintained by limited portions of blue laser irradiation. Blue laser irradiation should be applied at a level that increases the spectrometric analysability but does not negatively affect the qualitative properties of the deposition track.

Conclusion

Laser cladding experiments have been performed using a NIR high power diode laser and a blue high power diode laser. Experiments have been carried out with both wavelengths individually and simultaneously in the mix. Spectrometric

measurements have been performed during the DED process. Deposition track samples have been analysed by measuring cross-sectional-dimensions and determining of element distribution using XPS. The following is concluded from the work in this article:

- The use of blue laser radiation leads to much higher increase of the spectrometric signals. Hence, a portion of blue laser radiation mixed into the process might be a suitable enabler for spectrometric in-line investigation purposes.
- Dilution with the substrate correlates with the amount of base material content found on the surface of the cladding. Hence, the homogeneity is given in the cladding for both wavelengths.
- It is possible to produce comparable results in terms of cladding quality independently from the wavelength.
- Aiming for the same results in geometrical factors like welding depth and track height, the blue laser radiation shows a higher efficiency. Less power (app. 30% less) is needed for the same amount of cladding.

A spectrometric analysis of the process is in general difficult due to the comparable low intensities used in laser cladding. However, as described above, using blue laser irradiation leads to higher amount of the well-evaluable Type-A spectra, while the cross-sectional-dimensions and element distribution can be maintained. This is also valid for just a mix of both wavelengths instead of using only the NIR-radiation. Hence, it is possible to enable in-line process analysis by adding blue laser irradiation to the mix of the beam. To our best knowledge, this is the first work on the application of both blue and NIR laser irradiation to DED processes. In order to verify the presented findings and identified trends or interrelationships, further extended experiments will be carried out in ongoing work.

Data Availability The datasets generated during and analysed during the current study are available from the corresponding author on reasonable request.

Declarations

Competing Interests The authors have no competing interests to declare that are relevant to the content of this article.

References

1. Kotarska, A., Poloczek, T., Janicki, D.: Characterization of the Structure, Mechanical Properties and Erosive Resistance of the Laser Cladded Inconel 625-Based Coatings Reinforced by TiC Particles. Materials (Basel, Switzerland) (2021). https://doi.org/10.3390/ma14092225

2. Seo, J.-W., Kim, J.-C., Kwon, S.-J., Jun, H.-K.: Effects of Laser Cladding for Repairing and Improving Wear of Rails. Int. J. Precis. Eng. Manuf. (2019). https://doi.org/10.1007/s12541-019-00115-y

3. Saboori, A., Aversa, A., Marchese, G., Biamino, S., Lombardi, M., Fino, P.: Application of Directed Energy Deposition-Based Additive Manufacturing in Repair. Appl. Sci. (2019). https://doi.org/10.3390/app9163316

4. Penaranda, X., Moralejo, S., Lamikiz, A., Figueras, J.: An adaptive laser cladding methodology for blade tip repair. Int. J. Adv. Manuf. Technol. (2017). https://doi.org/10.1007/s00170-017-0500-1

5. Lee, H., Lim, C.H.J., Low, M.J., Tham, N., Murukeshan, V.M., Kim, Y.-J.: Lasers in additive manufacturing: A review. Int. J. Precis. Eng. and Manuf.-Green Tech. (2017). https://doi.org/10.1007/s40684-017-0037-7

6. Frazier, W.E.: Metal Additive Manufacturing: A Review. J. Mater. Eng. Perform. (2014). https://doi.org/10.1007/s11665-014-0958-z

7. DebRoy, T., Wei, H.L., Zuback, J.S., Mukherjee, T., Elmer, J.W., Milewski, J.O., Beese, A.M., Wilson-Heid, A., De, A., Zhang, W.: Additive manufacturing of metallic components – Process, structure and properties. Prog. Mater Sci. (2018). https://doi.org/10.1016/j.pmatsci.2017.10.001

8. Mohan, D.G., Tomków, J., Karganroudi, S.S.: Laser Welding of UNS S33207 Hyper-Duplex Stainless Steel to 6061 Aluminum Alloy Using High Entropy Alloy as a Filler Material. Appl. Sci. (2022). https://doi.org/10.3390/app12062849

9. Köhler, H., Thomy, C., Vollertsen, F.: Contact-less temperature measurement and control with applications to laser cladding. Weld. World (2016). https://doi.org/10.1007/s40194-015-0275-7

10. Doubenskaia, M., Pavlov, M., Grigoriev, S., Smurov, I.: Definition of brightness temperature and restoration of true temperature in laser cladding using infrared camera. Surf. Coat. Technol. (2013). https://doi.org/10.1016/j.surfcoat.2012.10.044

11. Bi, G., Gasser, A., Wissenbach, K., Drenker, A., Poprawe, R.: Identification and qualification of temperature signal for monitoring and control in laser cladding. Opt. Lasers Eng. (2006). https://doi.org/10.1016/j.optlaseng.2006.01.009

12. Song, L., Mazumder, J.: Feedback Control of Melt Pool Temperature During Laser Cladding Process. IEEE Trans. Contr. Syst. Technol. (2011). https://doi.org/10.1109/TCST.2010.2093901

13. Altenburg, S.J., Maierhofer, C., Straße, A., Gumenyuk, A.: Comparison of MWIR thermography and high-speed NIR thermography in a laser metal deposition (LMD) process. In: Proceedings of the 2018 International Conference on Quantitative InfraRed Thermography. 2018 Quantitative InfraRed Thermography. QIRT Council. https://doi.org/10.21611/qirt.2018.p35

14. Thawari, N., Gullipalli, C., Chandak, A., Gupta, T.V.K.: Influence of laser cladding parameters on distortion, thermal history and melt pool behaviour in multi-layer deposition of stellite 6: In-situ measurement. J. Alloy. Compd. (2021). https://doi.org/10.1016/j.jallcom.2020.157894

15. Chua, Z.Y., Ahn, I.H., Moon, S.K.: Process monitoring and inspection systems in metal additive manufacturing: Status and applications. Int. J. Precis. Eng. Manuf.-Green Tech. (2017). https://doi.org/10.1007/s40684-017-0029-7

16. Chabot, A., Rauch, M., Hascoët, J.-Y.: Towards a multi-sensor monitoring methodology for AM metallic processes. Weld. World (2019). https://doi.org/10.1007/s40194-019-00705-4

17. Buhr, M., Weber, J., Wenzl, J.-P., Möller, M., Emmelmann, C.: Influences of process conditions on stability of sensor controlled robot-based laser metal deposition. Procedia CIRP (2018). https://doi.org/10.1016/j.procir.2018.08.067

18. Huber, S.: In-situ-Legierungsbestimmung beim Laserstrahlschweißen. Zugl.: München, Techn. Univ., Diss., 2014. Forschungsberichte IWB, vol. 286. Utz, München (2014)

19. Vetter, K., Murken, N., Winkel, T., Freiße, H., Bohlen, A., Vollertsen, F.: Qualitätssicherung mittels Spektroskopie bei der laserbasierten experimentellen Werkstoffentwicklung. Quelle: Werkstoffe in der Fertigung **1**, 27–20 (2020). https://werkstoffzeitschrift.de/qualitaetssicherung-mittels-spektroskopie-bei-der-laserbasierten-experimentellen-werkstoffentwicklung/

20. Sibillano, T., Ancona, A., Berardi, V., Lugarà, P.M.: A real-time spectroscopic sensor for monitoring laser welding processes. Sensors (Basel, Switzerland) (2009). https://doi.org/10.3390/s90503376

21. Kong, F., Ma, J., Carlson, B., Kovacevic, R.: Real-time monitoring of laser welding of galvanized high strength steel in lap joint configuration. Opt. Laser Technol. (2012). https://doi.org/10.1016/j.optlastec.2012.03.003

22. Norman, P., Engström, H., Kaplan, A.F.H.: Theoretical analysis of photodiode monitoring of laser welding defects by imaging combined with modelling. J. Phys. D: Appl. Phys. (2008). https://doi.org/10.1088/0022-3727/41/19/195502

23. Rizzi, D., Sibillano, T., Pietro Calabrese, P., Ancona, A., Mario Lugarà, P.: Spectroscopic, energetic and metallographic investigations of the laser lap welding of AISI 304 using the response surface methodology. Opt. Lasers Eng. (2011). https://doi.org/10.1016/j.optlaseng.2011.02.014

24. Montazeri, M., Nassar, A.R., Stutzman, C.B., Rao, P.: Heterogeneous sensor-based condition monitoring in directed energy deposition. Addit. Manuf. (2019). https://doi.org/10.1016/j.addma.2019.100916

25. Stutzman, C.B., Nassar, A.R., Reutzel, E.W.: Multi-sensor investigations of optical emissions and their relations to directed energy deposition processes and quality. Addit. Manuf. (2018). https://doi.org/10.1016/j.addma.2018.03.017

26. Nassar, A.R., Spurgeon, T.J., Reutzel, E.W.: Sensing defects during directed-energy additive manufacturing of metal parts using optical emissions spectroscopy. In 25th Annual International Solid Freeform Fabrication Symposium An Additive Manufacturing Conference. SFF **2014**, 278–287 (2014)

27. Kramida, A., Ralchenko, Y.: NIST Atomic Spectra Database, NIST Standard Reference Database 78 (1999). Accessed 6 April 2021

28. Bartkowiak, K.: Direct laser deposition process within spectrographic analysis in situ. Phys. Procedia (2010). https://doi.org/10.1016/j.phpro.2010.08.090

29. Kisielewicz, A., Sadeghi, E., Sikström, F., Christiansson, A.-K., Palumbo, G., Ancona, A.: In-process spectroscopic detection of chromium loss during Directed Energy Deposition of alloy 718. Mater. Des. (2020). https://doi.org/10.1016/j.matdes.2019.108317

30. Schmidt, M., Huke, P., Gerhard, C., Partes, K.: In-Line Observation of Laser Cladding Processes via Atomic Emission Spectroscopy. Materials (Basel, Switzerland) (2021). https://doi.org/10.3390/ma14164401

31. Schmidt, M., Gorny, S., Rüssmeier, N., Partes, K.: Investigation on laser cladding processes using high-resolution in-line atomic emission spectroscopy. In: DVS Media GmbH (ed.) Conference: ITSC 2022 Thermal Spray Conference and Exposition. DVS-Berichte, pp. 876–883. DVS Media GmbH, Düsseldorf

32. Dunbar, A.J., Nassar, A.R.: Assessment of optical emission analysis for in-process monitoring of powder bed fusion additive manufacturing. Virtual Phys. Prototyp. (2018). https://doi.org/10.1080/17452759.2017.1392683

33. Lough, C.S., Escano, L.I., Qu, M., Smith, C.C., Landers, R.G., Bristow, D.A., Chen, L., Kinzel, E.C.: In-situ optical emission spectroscopy of selective laser melting. J. Manuf. Process. (2020). https://doi.org/10.1016/j.jmapro.2020.02.016

34. Song, L., Mazumder, J.: Real Time Cr Measurement Using Optical Emission Spectroscopy During Direct Metal Deposition Process. IEEE Sensors J. (2012). https://doi.org/10.1109/JSEN.2011.2162316

35. Shin, J., Mazumder, J.: Composition monitoring using plasma diagnostics during direct metal deposition (DMD) process. Opt. Laser Technol. (2018). https://doi.org/10.1016/j.optlastec.2018.03.020

36. Wang, S., Liu, C.: Real-Time Monitoring of Chemical Composition in Nickel-Based Laser Cladding Layer by Emission Spectroscopy Analysis. Materials (Basel, Switzerland) (2019). https://doi.org/10.3390/ma12162637

37. Song, L., Huang, W., Han, X., Mazumder, J.: Real-Time Composition Monitoring Using Support Vector Regression of Laser-Induced Plasma for Laser Additive Manufacturing. IEEE Trans. Ind. Electron. (2017). https://doi.org/10.1109/TIE.2016.2608318

38. Britten, S.W., Schmid, L., Molitor, T., Rütering, M.: Blue high-power laser sources for processing solutions in e-mobility and beyond. Procedia CIRP (2020). https://doi.org/10.1016/j.procir.2020.09.082

39. Maina, M.R., Okamoto, Y., Hamada, K., Okada, A., Nakashiba, S.-I., Nishi, N.: Effects of superposition of 532 nm and 1064 nm wavelengths in copper micro-welding by pulsed Nd:YAG laser. J. Mater. Process. Technol. (2022). https://doi.org/10.1016/j.jmatprotec.2021.117388

40. Stritt, P., Hagenlocher, C., Kizler, C., Weber, R., Rüttimann, C., Graf, T.: Laser Spot Welding of Copper-aluminum Joints Using a Pulsed Dual Wavelength Laser at 532 and 1064nm. Phys. Procedia (2014). https://doi.org/10.1016/j.phpro.2014.08.083

41. Hummel, M., Schöler, C., Häusler, A., Gillner, A., Poprawe, R.: New approaches on laser micro welding of copper by using a laser beam source with a wavelength of 450 nm. J. Adv. Join. Process. (2020). https://doi.org/10.1016/j.jajp.2020.100012

42. Yang, H., Tang, X., Hu, C., Liu, S., Fan, Y., Xiao, Y., Lu, G., Wang, Q., Chen, G., Xing, P., Tan, H., Guo, Z., Niu, Z.: Study on laser welding of copper material by hybrid light source of blue diode laser and fiber laser. J. Laser Appl. (2021). https://doi.org/10.2351/7.0000386

43. Cui, L., Chen, B., Chen, L., He, D.: Dual beam laser keyhole welding of steel/aluminum lapped joints. J. Mater. Process. Technol. (2018). https://doi.org/10.1016/j.jmatprotec.2018.02.016

44. Li, Y., Zhu, Z., Tang, X., Han, S., Zhang, R., Cui, H.: Improvement of welding stability and mechanical properties of galvanized DP800 steel lap joint by high-speed tandem beam laser. Opt. Laser Technol. (2022). https://doi.org/10.1016/j.optlastec.2022.107958

45. Steen, W.M., Mazumder, J.: Laser Material Processing. Springer, London, London (2010)

46. Trichili, A., et al.: Retrofitting FSO Systems in Existing RF Infrastructure: A Non-Zero-Sum Game Technology. In IEEE Open Journal of the Communications Society. 2, 2597–2615 (2021). https://doi.org/10.1109/OJCOMS.2021.3130645

47. Johnson, P., Christy, R.: Optical constants of transition metals: Ti, V, Cr, Mn, Fe Co, Ni, and Pd. Phys. Rev. B (1974). https://doi.org/10.1103/PhysRevB.9.5056

48. Liu, S., Zhang, Y., Kovacevic, R.: Numerical Simulation and Experimental Study of Powder Flow Distribution in High Power Direct Diode Laser Cladding Process. Lasers Manuf. Mater. Process. (2015). https://doi.org/10.1007/s40516-015-0015-2

49. Black, D.L., McQuay, M.Q.: Laser-based particle measurements of spherical and nonspherical particles. Int. J. Multiph. Flow (2001). https://doi.org/10.1016/S0301-9322(01)00008-8

50. Wallace, L., Hinkle, K.: THE 236.6–5400.0 nm SPECTRUM OF Cr I. ApJ (2009). https://doi.org/10.1088/0004-637X/700/1/720

51. Nave, G., Johansson, S., Learner, R.C.M., Thorne, A.P., Brault, J.W.: A new multiplet table for Fe I. ApJS (1994). https://doi.org/10.1086/192079

52. Janssen, B.H., Pillen, S., Voet, N.B.M., Heerschap, A., van Engelen, B.G.M., van Alfen, N.: Quantitative muscle ultrasound versus quantitative magnetic resonance imaging in facioscapulohumeral dystrophy. Muscle Nerve (2014). https://doi.org/10.1002/mus.24247

Authors and Affiliations

Malte Schmidt[1] · **Robert Köhler[2]** · **Christoph Gerhard[2,3]** · **Knut Partes[1]**

✉ Malte Schmidt
    malte.schmidt@jade-hs.de

   Robert Köhler
   robert.koehler@hawk.de

   Christoph Gerhard
   christoph.gerhard@hawk.de; christoph.gerhard@polimi.it

   Knut Partes
   knut.partes@jade-hs.de

1   Department of Engineering Sciences, Jade University of Applied Sciences,
    Friedrich-Paffrath-Str. 101, 26389 Wilhelmshaven, Germany

2   Faculty of Engineering and Health, University of Applied Sciences and Arts,
    Von-Ossietzky-Straße 99, 37085 Göttingen, Germany

3   School of Industrial and Information Engineering, Politecnico Di Milano, Piazza Leonardo da
    Vinci 32, 20133 Milan, Italy